Supporting information

Nanoscale mapping of the 3D strain tensor in a germanium quantum well hosting a functional spin qubit device

Cedric Corley-Wiciak[1], Carsten Richter[2], Marvin H. Zoellner[1], Ignatii Zaitsev[1], Costanza L. Manganelli[1], Edoardo Zatterin [3], Tobias U. Schülli[3], Agnieszka A. Corley-Wiciak[1], Jens Katzer [1], Felix Reichmann[1], Wolfgang M. Klesse[1], Nico W. Hendrickx[4], Amir Sammak[5], Menno Veldhorst[4], Giordano Scappucci[4], Michele Virgilio[6], Giovanni Capellini[1,7]

[1] IHP – Leibniz-Institut für innovative Mikroelektronik, Im Technologiepark 25, D-15236 Frankfurt(Oder), Germany
[2] IKZ – Leibniz -Institut für Kristallzüchtung, Max-Born-Straße 2, D-12489 Berlin, Germany
[3] ESRF – European Synchrotron Radiation Facility, 71, avenue des Martyrs, CS 40220, 38043 Grenoble Cedex 9, France
[4] QuTech and Kavli Institute of Nanoscience, Delft University of Technology, Lorentzweg 1, 2628 CJ Delft, The Netherlands
[5] QuTech and Netherlands Organisation for Applied Scientific Research (TNO), Stieltjesweg 1, 2628 CK Delft, The Netherlands
[6] Department of Physics Enrico Fermi, Università di Pisa, Pisa 56126, Italy
[7] Dipartimento di Scienze, Universita Roma Tre, Roma 00146, Italy

Corresponding Author: Tel. +49 335 5625 179; E-mail adress: corley@ihp-microelectronics.com (C. Corley-Wiciak)

SXDM data analysis

In this section, we describe how the raw data obtained for our strain mapping experiment was processed to provide the diffraction maps shown in Figure 3 in the main text.

We recorded SXDM datasets with a Field of View (FOV) of 5 x 5 μm^2 at a lateral step size of 40 nm around the qubit device for the 335, $\bar{3}\bar{3}5$ and $3\bar{3}5$ Bragg reflections. For each reflection, a dataset is based on 2D raster scans (x, y) of the sample through the nano-focused beam while an area detector ($Maxipix$[6], 516×516 px) is read out each 30 ms, recording a 2D distribution of diffracted X-rays. These scans produce 4D datasets, since the detector image represents a 2D cut through reciprocal space. To obtain a 3D reciprocal space map for each point on the sample, the rasters were iterated for a series of rocking angles ω. Thus, a 5D dataset is obtained. Switching between the reflections was achieved by rotating the sample by 90° about the azimuthal angle φ. The data acquisition took approx. 15 h, not including the time needed for sample alignment.

From the raw data, maps of the scattering vectors for the Ge QW layer for each reflection ($\mathbf{Q}_{335}$, $\mathbf{Q}_{\bar{3}\bar{3}5}$, $\mathbf{Q}_{3\bar{3}5}$) have to be determined in a multi-step analysis procedure. First, for each reflection, the series of raster scan has to be corrected for drift. During the measurement, the sample moves (1) with time due to settling of motors or thermal drifts, and (2) with ω due to any offset between the rotation axis of ω and the beam spot on the sample. The magnitude of this movement is typically around 1 µm per degree in ω, and around 1.5 µm total in our measurement. Thus, the 4D diffraction maps for consecutive steps in ω have to be shifted relative to each other in real space. For the drift correction, we used the *python*-based *X-ray Strain Orientation Calculation Software (X-SOCS)*, developed at ID01. In *X-SOCS*, the drift of a series of raster scans is assessed by tracking the positions of selected features on the sample in dependence on ω.
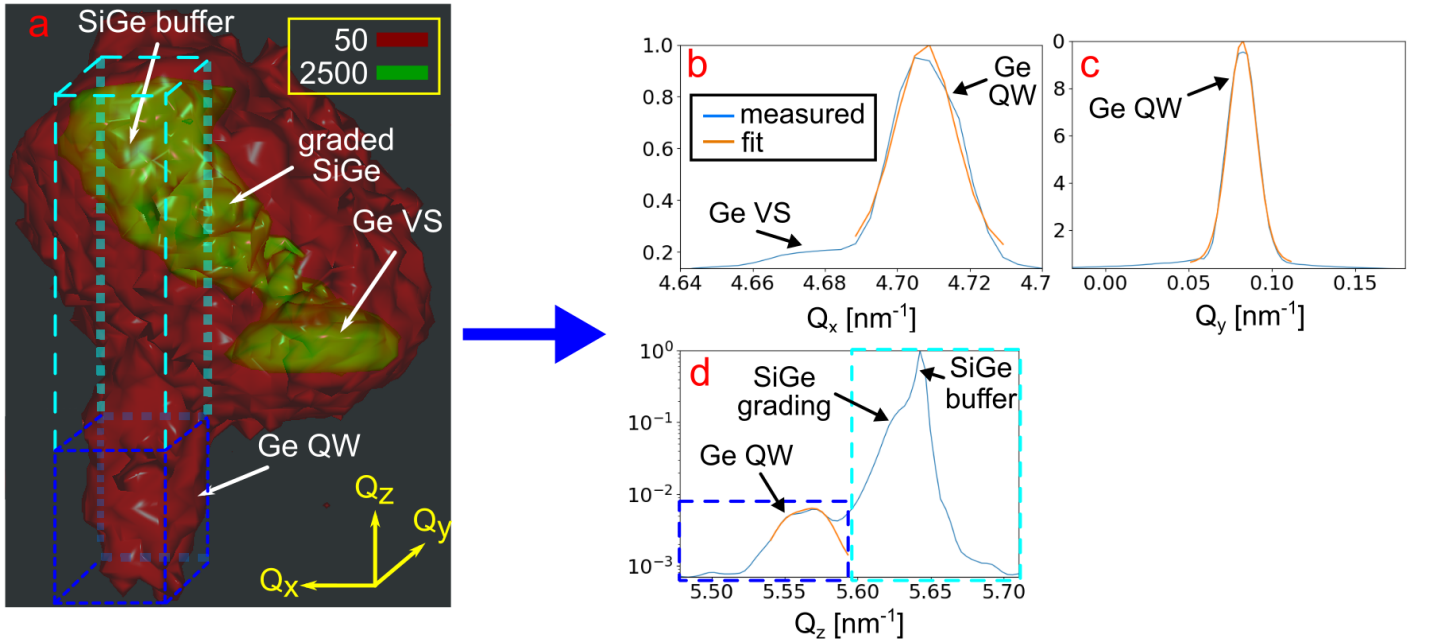

Figure S1 Three-dimensional Reciprocal Space Map of the Ge/SiGe hole spin qubit heterostructure and projections of the scattering vector for the Ge QW layer. **(a)** Isosurface plot of the 3D RSM with the ROI used to isolate the Ge QW layer signal. The relative intensities of the isosurfaces are described by the legend (in arbitrary units); **(b, c, d)** Averaged projections of the normalized scattered intensity from the Ge QW layer along Q_x, Q_y, Q_z. (Blue curves) measured intensity; (Orange curve) Fits with Pseudo Voigt functions.

In the next step, for each sample position, a series of 2D detector images at different rocking angles ω was converted into 3D Cartesian reciprocal space (Q_x, Q_y, Q_z). We defined the Cartesian reference system with respect to the Ge crystal lattice: $\mathbf{Q}_x \parallel [1\ 1\ 0]$, $\mathbf{Q}_y \parallel [1\ \bar{1}\ 0]$, $\mathbf{Q}_z \parallel [0\ 0\ 1]$, where $[0\ 0\ 1]$ is the nominal direction of the surface normal. In this reference system, the Bragg reflections of the $\{3\ 3\ 5\}$ family will always be located close to one of the in-plane axes ($Q_x \approx 0$ or $Q_y \approx 0$). The conversion was be achieved using *X-SOCS*, based on the X-ray energy as well as the sample-detector distance and the detector pixel size. A 3D rendering of the thus obtained 3D RSM for a specific point on the sample is shown in Figure S1a.

The next steps aims at reducing the 5D dataset $I(x, y, Q_x, Q_y, Q_z)$ to a 3D vector field of the kind $\mathbf{Q}_{QW} = (Q_{x,QW}, Q_{y,QW}, Q_{z,QW})$ by determining the Bragg peak position of the QW layer within the 3D RSMs. This step is iterated over all (x, y) sample positions and was based on custom *python* scripts. It involves an optimized, automated peak fitting procedure required due to significant overlap of the QW layer peak with diffraction from the thick, graded $Si_{0.2}Ge_{0.8}$ buffer layer (dashed light blue box in Figure S1a), which is 2-3 orders of magnitude more intense. To isolate the QW layer peak, we selected a 3D region of interest (ROI) around it (solid dark blue box) and further studied its 1D projections onto the three Cartesian recip-

rocal axes $(I(Q_x), I(Q_y), I(Q_z)$ – blue curves in Figure S1b-d). The center positions of the peak are determined by fitting a suitable profile (orange curves).

For the in-plane directions $Q_{x,QW}$ and $Q_{y,QW}$, fitting a standard Pseudo Voigt function was sufficient, while for the out-of-plane direction $Q_{z,QW}$, obtaining a good fit was more challenging due to the described peak overlap and an intensity modulation caused by the interferences from the interfaces within the pseudomorphic SiGe/Ge/SiGe stack. To resolve the latter, we modeled the QW peak by a sum of two Pseudo Voigt profiles with different center positions instead of a single profile. The whole procedure was done in a loop iterating over all sample position, thus yielding 2D spatial maps for all components of the scattering vector of the Ge QW layer. These are exemplarily shown for the 335 Bragg reflection in Figure S2.
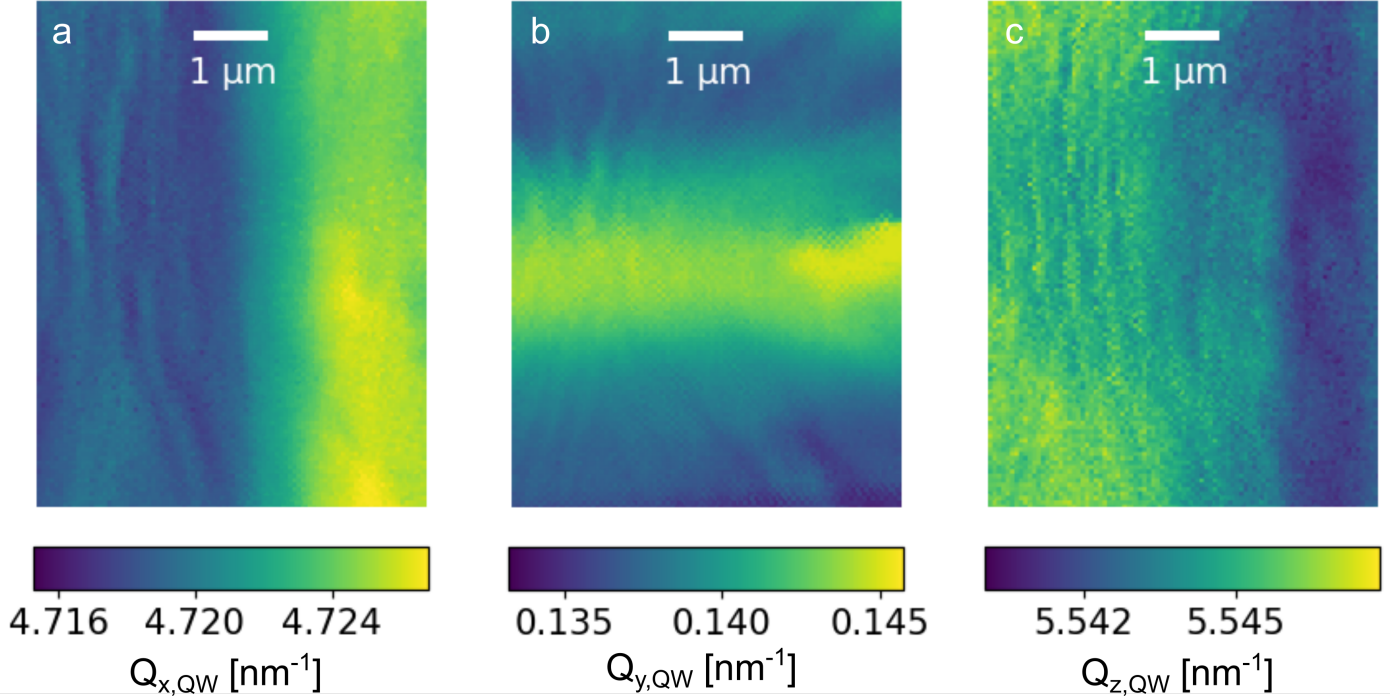
Figure S2 Maps of the three components of the scattering vector of the 335 reflection. (a) Map of $Q_{x,QW}$; (b) Map of $Q_{y,QW}$; (c) Map of $Q_{z,QW}$

We note that the errors for $Q_{x,QW}$, $Q_{y,QW}$, $Q_{z,QW}$ vary locally depending on the goodness of the fits and the statistical error. The fit errors are a limiting factor for the overall sensitivity of the SXDM technique in the presence of peak overlap. In our datasets, on average, the fitting errors for $Q_{x,QW}$ and $Q_{y,QW}$ are in the range of $3 \ldots 5 \times 10^{-4}\,\mathrm{nm}^{-1}$, while the error for $Q_{z,QW}$ is typically around $7 \ldots 10 \times 10^{-4}\,\mathrm{nm}^{-1}$. Furthermore, a systematic offset in the RSMs may occur due to an imperfect alignment of sample or diffractometer. We corrected this offset by comparing a reference measurement obtained by lab XRD with the average over all frames of the SXDM dataset.

The data analysis procedure described up to here is performed separately for each of the three {335} Bragg reflections. The resulting maps of the total length (modulus) of the scattering vector $|\mathbf{Q}|$ are shown in Figure 3 in the main text. In the next step, the diffraction maps $\mathbf{Q}_{QW}$ for the three Bragg reflections are overlaid and a linear combination of the scattering vectors is performed for every (x, y) sample position. Superimposing the diffraction maps allows for the local calculation of pseudo scattering vectors along the Cartesian reciprocal directions of interest $(110, 1\bar{1}0, 001)$ as follows:[13;7]

$$\mathbf{Q}_{001} = \frac{1}{10} \cdot \left(\mathbf{Q}_{335} + \mathbf{Q}_{\bar{3}\bar{3}5} \right), \tag{1}$$

$$\mathbf{Q}_{110} = \frac{1}{6} \cdot \left(\mathbf{Q}_{335} - \mathbf{Q}_{\bar{3}\bar{3}5} \right), \tag{2}$$

$$\mathbf{Q}_{1\bar{1}0} = \frac{1}{3} \cdot \left(\mathbf{Q}_{3\bar{3}5} - 5 \cdot \mathbf{Q}_{001} \right). \tag{3}$$

From $\mathbf{Q}_{110}, \mathbf{Q}_{1\bar{1}0}$ and $\mathbf{Q}_{001}$, the corresponding real space basis vectors $\mathbf{R}_{110}, \mathbf{R}_{1\bar{1}0}$ and $\mathbf{R}_{001}$ are obtained by

$$\mathbf{R}_{110} = 2\pi \cdot \frac{\mathbf{Q}_{001} \times \mathbf{Q}_{1\bar{1}0}}{\mathbf{Q}_{110} \cdot \mathbf{Q}_{001} \times \mathbf{Q}_{1\bar{1}0}}, \tag{4}$$

$$\mathbf{R}_{1\bar{1}0} = 2\pi \cdot \frac{\mathbf{Q}_{110} \times \mathbf{Q}_{001}}{\mathbf{Q}_{1\bar{1}0} \cdot \mathbf{Q}_{110} \times \mathbf{Q}_{001}}, \tag{5}$$

$$\mathbf{R}_{001} = 2\pi \cdot \frac{\mathbf{Q}_{1\bar{1}0} \times \mathbf{Q}_{110}}{\mathbf{Q}_{001} \cdot \mathbf{Q}_{1\bar{1}0} \times \mathbf{Q}_{110}}, \tag{6}$$

The moduli of the real space lattice vectors correspond directly to the three (virtual) lattice parameters $a_{110}, a_{1\bar{1}0}, a_{001}$:

$$a_{110} = \sqrt{2} \cdot |\mathbf{R}_{110}|, \tag{7}$$

$$a_{1\bar{1}0} = \sqrt{2} \cdot |\mathbf{R}_{1\bar{1}0}|, \tag{8}$$

$$a_{001} = |\mathbf{R}_{010}|. \tag{9}$$

Thus, for convenience, we defined a virtual unit cell that is rotated by $45°$ about the surface normal with respect to the Ge unit cell. This choice is based on the principal directions of misfit dislocations and the device layout. The three angular lattice constants α, β, γ are then calculated from the angles between $\mathbf{R}_{110}, \mathbf{R}_{1\bar{1}0}, \mathbf{R}_{001}$:

$$\alpha = \arccos\left(\frac{\mathbf{R}_{001} \cdot \mathbf{R}_{1\bar{1}0}}{|\mathbf{R}_{001}| \cdot |\mathbf{R}_{1\bar{1}0}|}\right), \tag{10}$$

$$\beta = \arccos\left(\frac{\mathbf{R}_{001} \cdot \mathbf{R}_{110}}{|\mathbf{R}_{001}| \cdot |\mathbf{R}_{110}|}\right), \tag{11}$$

$$\gamma = \arccos\left(\frac{\mathbf{R}_{110} \cdot \mathbf{R}_{1\bar{1}0}}{|\mathbf{R}_{110}| \cdot |\mathbf{R}_{1\bar{1}0}|}\right), \tag{12}$$

This way, the full set of six lattice parameters is obtained for every spot on the map, allowing to calculate the spatially dependent strain tensor by the equations (1) - (6) in the results section of the main text. Furthermore, the angle between the reciprocal in-plane axes γ^*, which depends on the lattice parameters of direct space, is introduced for convenience:

$$\gamma^* = \arccos\left(\frac{\cos\alpha \cdot \cos\beta - \cos\gamma}{|\sin\alpha| \cdot |\sin\beta|}\right). \tag{13}$$

The lattice strains are then calculated from the lattice constants according to equations 1-6 in the main text. The unfiltered strain maps determined by this analysis procedure are shown in Figure S3.
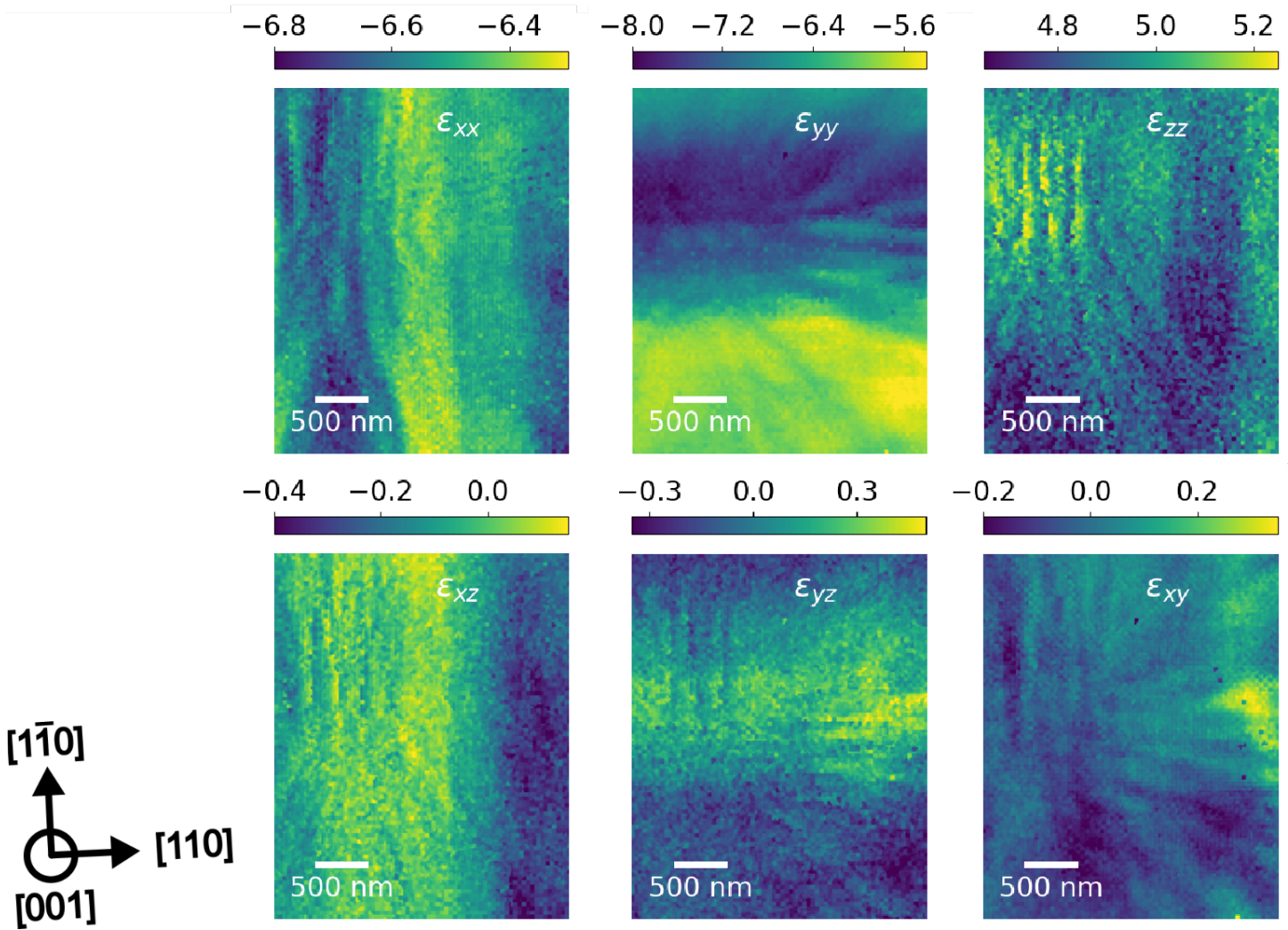
Figure S3 Unfiltered maps of the six components of the strain tensor in the vicinity of the qubits. **(Top row)** Maps of the three components on the main diagonal of the tensor. **(Bottom row)** Maps of the three shear strain components. The colorbars describe the magnitude of the strain in multiples of 10^{-3}. The orientations of the lattice planes are described by the black arrows.

The long-range gradients, which are caused by the dislocation networks in the buffer layers, may be filtered out by applying a 2D high-pass Fourier filter, highlighting the additional strain caused by the electrodes, as seen in Figure 5b in the main text. Likewise, the effect of the electrodes can be removed by applying a low-pass Fourier filter, to study exclusively the long-ranged strain fluctuations.

We note that the lateral spatial resolution of the SXDM measurement is governed by the size of the X-ray spot on the sample, which is found to be < 30 nm (see X-ray nanoprobe section) and the lateral step size of 40 nm used in the mapping. A further blurring is expected due to both the drift correction and the overlaying of the maps from different Bragg reflections. Thus, features with a lateral width of less or even slightly larger than 40 nm may not be fully resolved in the SXDM maps.

The errors for the strains are difficult to determine and mostly due to the statistical error of the fit of the partially overlapping Bragg peaks (Ge QW layer and the (graded) SiGe buffer) in reciprocal space. An attempt to estimate the confidence intervals for the strains is made based on the local fit errors for $Q_{x,QW}$, $Q_{y,QW}$, $Q_{z,QW}$ returned by the optimization routine. Based on the locally determined confidence interval, we propagate the error by inserting the confidence limits into the equations to calculate the strain tensor for each (x, y) sample position. We regard the difference between the maximum and minimum of strain obtained by this method as its confidence interval. In Figure 6a-b in the main text, the local confidence intervals of 3σ obtained thus for ε_{xx} and ε_{zz} are represented by the areas shaded in yellow.

Lattice rotations

The methodology presented in this work allows not only to calculate the strains of the crystal lattice, but also the three lattice rotations pitch η, roll χ, twist ϕ, which are illustrated in Figure 4a together with all strains in an orthorombic unit cell. To define the rotations, a set of reference unit vectors $\mathbf{v}$ along the main directions of the crystal lattice are calculated
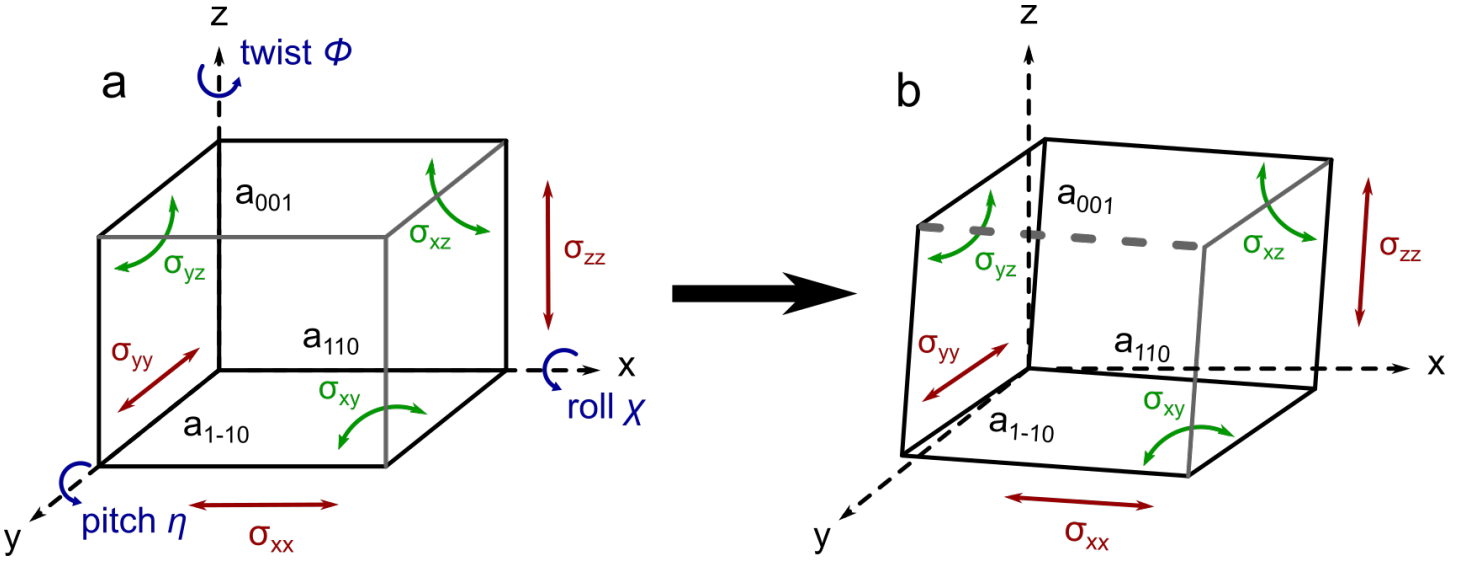
Figure S4 Schematic of the lattice deformations in a stressed and rotated orthorombic unit cell. (a) Unit cell with the deformations (red) Normal stresses; (green) shear stresses; (blue) lattice rotations. (b) Unit cell after rotation, which changes the orientation of stresses relative to the lattice planes.

from the global, lateral average of the lattice vectors $< \mathbf{R}_{001>}$, $< \mathbf{R}_{110>}$, $< \mathbf{R}_{1\bar{1}0>}$ to determine a reference system, with respect to which rotations are defined:

$$\mathbf{v}_{001} = \frac{< \mathbf{R}_{001} >}{| < \mathbf{R}_{001} > |} \; , \; \mathbf{v}_{110} = \frac{< \mathbf{R}_{110} >}{| < \mathbf{R}_{110} > |} \; , \; \mathbf{v}_{1\bar{1}0} = \frac{< \mathbf{R}_{1\bar{1}0} >}{| < \mathbf{R}_{1\bar{1}0} > |}$$

$$\mathbf{v}_{111} = \frac{\mathbf{v}_{001} + \mathbf{v}_{110}}{|\mathbf{v}_{001} + \mathbf{v}_{110}|} \tag{14}$$

$$\mathbf{v}_{1\bar{1}1} = \frac{\mathbf{v}_{001} + \mathbf{v}_{1\bar{1}0}}{|\mathbf{v}_{001} + \mathbf{v}_{1\bar{1}0}|} \tag{15}$$

$$\mathbf{v}_{100} = \frac{1}{2} \cdot \frac{\mathbf{v}_{110} + \mathbf{v}_{1\bar{1}0}}{|\mathbf{v}_{110} + \mathbf{v}_{1\bar{1}0}|} \tag{16}$$

The rotations are calculated as the sum of two angles, each between one vector from $\{\mathbf{R}_{110}, \mathbf{R}_{1\bar{1}0}, \mathbf{R}_{001}\}$ and one reference vector $\{\mathbf{v}_{111}, \mathbf{v}_{1\bar{1}1}, \mathbf{v}_{100}\}$:

$$\eta = \frac{1}{2} \cdot (\arccos(\mathbf{R}_{001} \cdot \mathbf{v}_{111}) - \arccos(\mathbf{R}_{110} \cdot \mathbf{v}_{111})) \, , \tag{17}$$

$$\chi = \frac{1}{2} \cdot (\arccos(\mathbf{R}_{001} \cdot \mathbf{v}_{1\bar{1}1}) - \arccos(\mathbf{R}_{1\bar{1}0} \cdot \mathbf{v}_{1\bar{1}1})) \, , \tag{18}$$

$$\phi = \frac{1}{2} \cdot (\arccos(\mathbf{R}_{110} \cdot \mathbf{v}_{100}) - \arccos(\mathbf{R}_{1\bar{1}0} \cdot \mathbf{v}_{100})) \tag{19}$$

The local rotations of the unit cells, as depicted in Figure S4b, change the orientation of the lattice planes relative to the directions along which stresses are applied, thus causing a local transformation of the stress tensor.[8] This leads to a translation of some amount of symmetric stress into shear stress, and moreover, the symmetric out-of-plane stress σ_{zz} may be non-zero in the rotated unit cell because the [001] direction is no longer parallel to the surface normal.

In Figure S5, the maps of the three lattice rotations calculated from the diffraction maps are shown. In $[1\bar{1}0]$ direction, the variation of the pitch η is small and caused only by the electrodes. However, there is a gradient in η of approx. 0.08 ° along [110] over a length scale of $l \sim 2$ μm related to the misfit network in the plastically-relaxed buffer layers. For χ, there is a slope along $[1\bar{1}0]$ similar in magnitude and length to the gradient of η along [110]. In [110] direction, the variation of χ is very small and caused only by the electrodes. Both the electrodes and the misfit dislocations appear to have an effect of a similar magnitude on the in-plane rotation ϕ, with (1) the electrodes causing abrupt local changes and (2) a slower gradient occurring along the slope of an undulation of the cross hatch pattern. We observe that the magnitude of long-ranged fluctuations in ϕ is smaller compared to those in η and χ by approximately a factor of five.
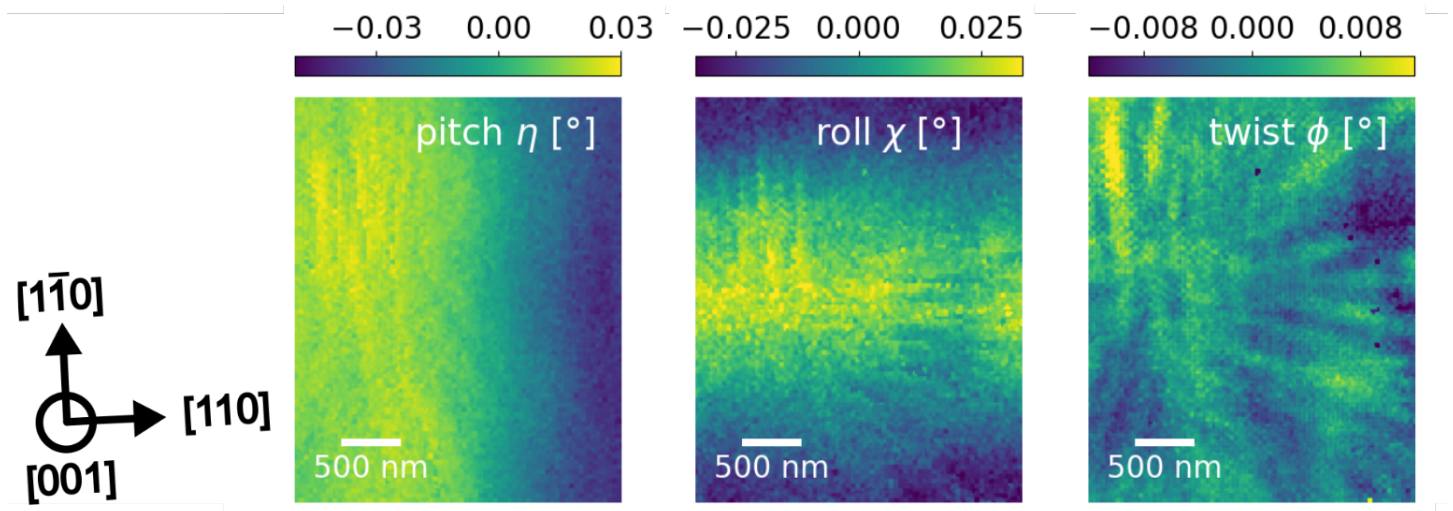
Figure S5 Maps of the lattice rotations. The colorbars are given in degrees. The orientations of the lattice planes are described by the black arrows.

Stiffness tensor and stress maps

In this section, we describe how the local lattice stresses are calculated from the strains measured by SXDM. In Voigt notation, the stress tensor $\underline{\sigma}$ in the Ge QW layer is calculated from the 6x6 stiffness tensor $\underline{\mathbf{C}}$, which has cubic symmetry and is well described in the literature,[5] and the experimentally determined strain tensor $\underline{\varepsilon}$.

In the literature, the stiffness tensor for materials in the cubic lattice system is typically given for the orientation $\mathbf{x}_{0°} = [100]$, $\mathbf{y}_{0°} = [010]$, $\mathbf{z}_{0°} = [001]$. However, we discuss the lattice strains along a more natural, rotated system: $\mathbf{x}_{45°} = [110]$, $\mathbf{y}_{45°} = [1\bar{1}0]$, $\mathbf{z}_{45°} = [001]$. Thus, we need to transform $\underline{\mathbf{C}}_{0°}$ by 45° rotation around [001] to gain the correct expression of the tensor $\underline{\mathbf{C}}_{45°}$ in our reference system. The two tensors $\underline{\mathbf{C}}_{0°}$ and $\underline{\mathbf{C}}_{45°}$ for Ge are given in equations (20) and (21) (in units of GPa).

$$
\underline{\mathbf{C}}_{0°} = \begin{bmatrix}
128.53 & 48.28 & 48.28 & 0 & 0 & 0 \\
48.28 & 128.53 & 48.28 & 0 & 0 & 0 \\
48.28 & 48.28 & 128.53 & 0 & 0 & 0 \\
0 & 0 & 0 & 68.3 & 0 & 0 \\
0 & 0 & 0 & 0 & 68.3 & 0 \\
0 & 0 & 0 & 0 & 0 & 68.3
\end{bmatrix}
\tag{20}
$$

$$
\underline{\mathbf{C}}_{45°} = \begin{bmatrix}
156.7 & 20.105 & 48.28 & 0 & 0 & 0 \\
20.105 & 156.7 & 48.28 & 0 & 0 & 0 \\
48.28 & 48.28 & 128.53 & 0 & 0 & 0 \\
0 & 0 & 0 & 68.3 & 0 & 0 \\
0 & 0 & 0 & 0 & 68.3 & 0 \\
0 & 0 & 0 & 0 & 0 & 40.125
\end{bmatrix}
\tag{21}
$$

Thus, we are able to calculate maps of all six independent components of $\underline{\sigma}$ in the Ge QW layer, shown in Figure S6, from $\underline{\mathbf{C}}_{45°}$ and the strain maps in Figure S3 according to Hooke's law in equation (22):[2]

$$
\underline{\sigma} = \underline{\mathbf{C}}_{45°} \cdot \underline{\varepsilon}
$$

$$
\begin{bmatrix}
\sigma_{xx} \\
\sigma_{yy} \\
\sigma_{zz} \\
\sigma_{yz} \\
\sigma_{xz} \\
\sigma_{xy}
\end{bmatrix} = \begin{bmatrix}
C_{11} & C_{12} & C_{13} & 0 & 0 & 0 \\
C_{21} & C_{22} & C_{23} & 0 & 0 & 0 \\
C_{31} & C_{32} & C_{33} & 0 & 0 & 0 \\
0 & 0 & 0 & C_{44} & 0 & 0 \\
0 & 0 & 0 & 0 & C_{55} & 0 \\
0 & 0 & 0 & 0 & 0 & C_{66}
\end{bmatrix} \begin{bmatrix}
\varepsilon_{xx} \\
\varepsilon_{yy} \\
\varepsilon_{zz} \\
2\varepsilon_{yz} \\
2\varepsilon_{xz} \\
2\varepsilon_{xy}
\end{bmatrix}
\tag{22}
$$

On average, the in-plane symmetric stresses σ_{xx} and σ_{yy} are approx. $\sigma_{xx} \approx \sigma_{yy} \approx 0.93$ GPa. In comparison, the average values for the out-of-plane symmetric stress σ_{zz} and the shear stresses σ_{xz} and σ_{yz}, which should be 0 in the ideal case for only biaxial stress, as well as σ_{xy}, are smaller by 2-3 orders of magnitude.

For a homogeneous thin film, typically no surface normal stress is assumed with $\sigma_{zz} = 0$. However, we observe local fluctuations of σ_{zz} of some tens of MPa in the Ge QW layer over both short and long length scales. For both effects, we consider a possible cause. The short-ranged fluctuations of σ_{zz} are also attributed to the electrodes. In areas underneath a metal strip, the Ge lattice is compressed along the in-plane directions and expands vertically in response (described in the main text), causing a curvature of the electrode which is counteracted by its stiffness. When the two forces exerted from the Ge lattice expansion and metal stiffness are in equilibrium, some amount of stress along the z-axis is present underneath the electrode, as seen in the σ_{zz} stress map.
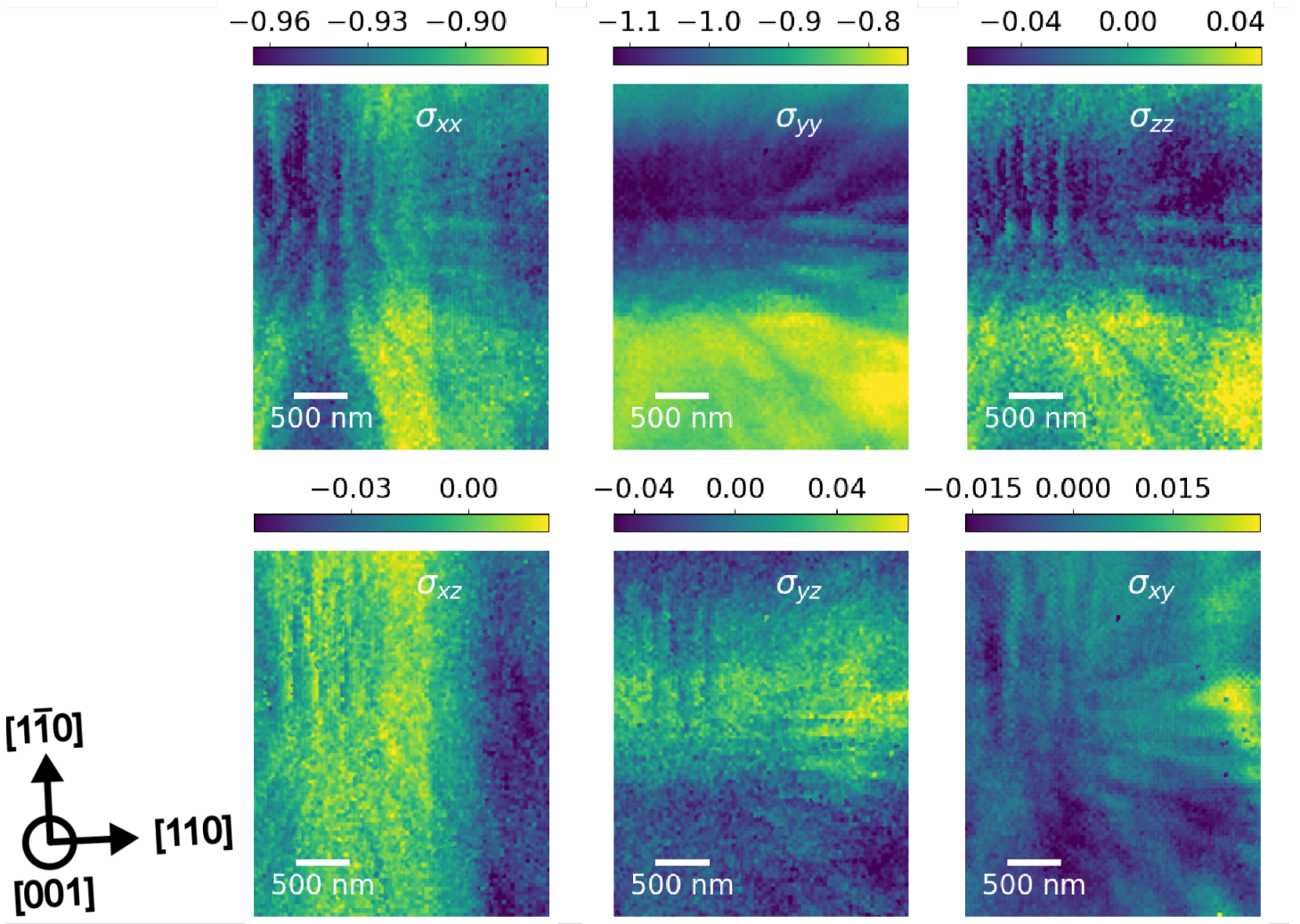
Figure S6 Maps of the six components of the stress tensor. The colorbars describe the magnitude of the stresses in GPa. The orientations of the lattice planes are described by the black arrows.

A potential contribution to long range gradients in σ_{zz} are local tilts of the lattice, which were described in the previous section of the supporting information. The Ge unit cells undergo local rotations, such that the [001] direction deviates from the surface normal, which results in a small magnitude of stress along this direction.

The spatial distribution of each stress component mostly matches to the corresponding strain component. An exception are the electrodes running mostly along [110] in the right side of the map, which are not well visible in ε_{zz} (see Figure 5 in the main text), but show a clear footprint in σ_{zz}. As noted in section 2.4 in the main text, the morphological and mechanical properties of the lithographically fabricated metal electrodes are affected by local inhomogeneities, such as grain boundaries. These effects may also influence the local stress exerted by the electrodes. We attribute these differences between ε_{zz} and σ_{zz} distribution to local inhomogeneities present in the electrodes.

Strain and composition in the buffer

In this section, we show SXDM measurements of strain and alloy composition in the 500 nm thick SiGe buffer layer. By applying the procedure described in the data analysis section to the SiGe scattering vector, we obtain the lattice constants in the SiGe buffer with lateral resolution. To calculate the lattice strains, the unstrained lattice constant a_0 of the $Si_{1-x}Ge_x$ unit cell is required, which depends on the composition x.

Since x undergoes local fluctuations, to obtain the strains we need to determine the local a_0, which is possible under the assumption of anisotropic biaxial stress with no stress along the surface normal. This assumption allows us to calculate a_0 by equation 23, which is derived from equation 22 for $\sigma_{zz} = 0$.

$$a_0 = \frac{\nu \cdot (a_{110} + a_{1\bar{1}0}) + (1 - \nu) \cdot a_{001}}{1 + \nu} \tag{23}$$

For this, we introduce the Poisson ratio ν, which depends on the elastic constants $C_{13} = C_{23}$ and C_{33} for SiGe.[12]

$$\nu = \frac{1}{\dfrac{C_{33}}{C_{13}} + 1} \tag{24}$$

With a_0, we can determine the components of the strain tensor according to equations 1-6 in the main text, and the local alloy composition x from the following equation 25 given by *Dismukes et. al*,[3] with the lattice constant of unstrained Silicon $a_{Si} = 5.431$ Å.

$$a_0 = a_{Si} \cdot (1 + 0.03683x + 0.00497x^2) \tag{25}$$
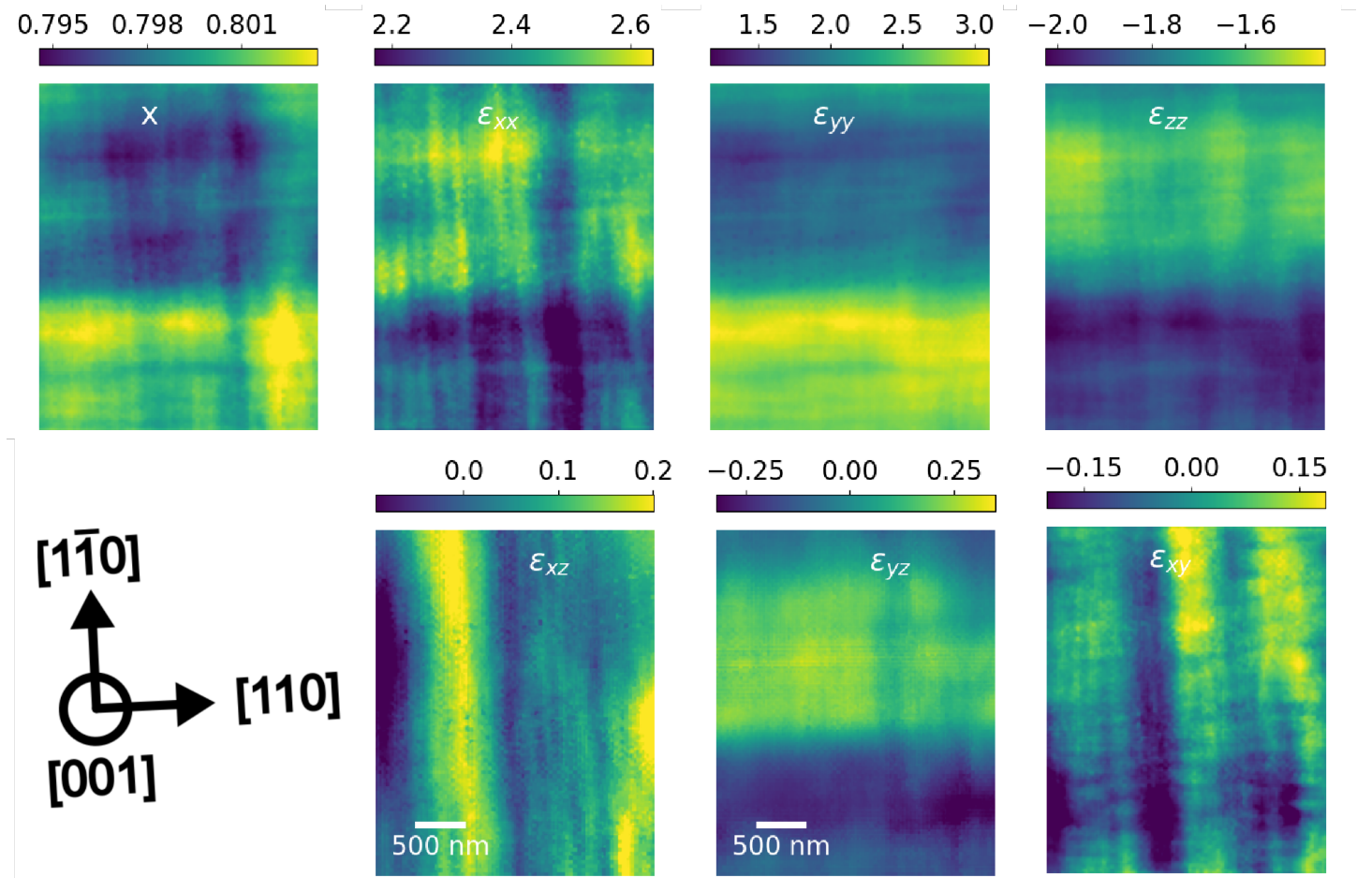
Figure S7 Maps of alloy composition and the strain tensor in the SiGe buffer layer. The colorbar of the composition map is dimensionless, the colorbar for the strain maps describes the strain in multiple of 10^{-3}

The maps for composition and strain are shown in Figure S7. The composition in the SiGe buffer is approx. $x = 79.9$ % om average, close to the nominal composition of $x = 80$ %. The average of the symmetric in-plane strains ε_{xx} and ε_{yy} is approx. $2.3 \cdot 10^{-3}$, which is a typical value for an epitaxial $Si_{0.2}Ge_{0.8}$ film grown at high temperature on a Ge VS, and stems from the mismatch between the thermal expansion coefficient of Ge and $Si_{0.2}Ge_{0.8}$.[11]

We notice that in all maps, we observe modulations in the form of sharp lines, reminiscent of the single misfit dislocation seen the diffraction map for the Ge QW layer (Figure 3c in the main text), and long-ranged gradients on a µm-scale. These fluctuations are caused by the dislocations mediating plastic relaxation at the lower interface of the SiGe layer,[1] The total magnitude of the modulations in the composition is approx. $x = 0.8$ % and in the strains approx. $1.8 \cdot 10^{-3}$. These values are in agreement with published findings from SXDM measurements on a thick relaxed SiGe buffer of a similar composition.[13]

We note that the lateral strain and composition distributions in a thick relaxed SiGe layer are depth-dependent, since the strain fields from these dislocations are cancelling out with distance to the interface at which the MD network is formed.[9] Thus, at given depth within the layer, the only contributions left are of a lateral wavelength corresponding to the vertical distance to the MD network (500 nm at the interface to the QW layer).

Since the SiGe X-ray diffraction signal is comprised of X-ray scattering from the entire thickness of the layer, the SXDM maps are comprised of the depth-average of the lateral variations of strain and composition. For this reason, we do not observe the footprint of the device on top of the structure, since the electrode-driven strain modulations are too weak to extent deeply into the sample. An interpretation of the MD-driven strain modulations apparent in these maps is possible by considering the depth-dependence of the wavelength of the strain distribution described above. We suggest that the sharp line-features stem from the region at the bottom of the SiGe layer, close to the MD network at the interface between Ge VS and SiGe, and attribute the long-ranged modulation to the top part of the SiGe layer, close to the interface of the Ge QW layer.

Excluding the effect of the electrodes, the strain in the Ge QW layer is defined by the in-plane lattice parameters of the SiGe at the lower interface of the QW layer, which is controlled by both in-plane strain and composition. We note that both ε_{yy} and x show an increase over a long range of $> 1 \ \mu$m from the top to the bottom of the map, similar to the ε_{yy} map for the Ge QW layer (Figure S3). Based on this qualitative observation, we conclude that there is a transfer of elastic strain from the composition and strain modulations in the SiGe buffer onto the Ge QW layer at its bottom interface. However, we maintain that the lateral extent of these modulations is on the µm scale and thus on a different spatial frequency than the electrode-driven strains, allowing a separation by Fourier-filtering.
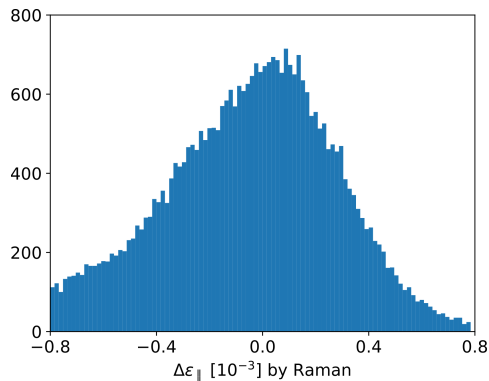
Histograms

In this section, we show histogramms of the strains in the Ge QW layer to demonstrate the bandwidth of their fluctuations. The distribution of the modulations stemming from the electrodes are shown in Figure S8 by the histogramms of the filtered SXDM strain maps (Figure 5b in the main text).
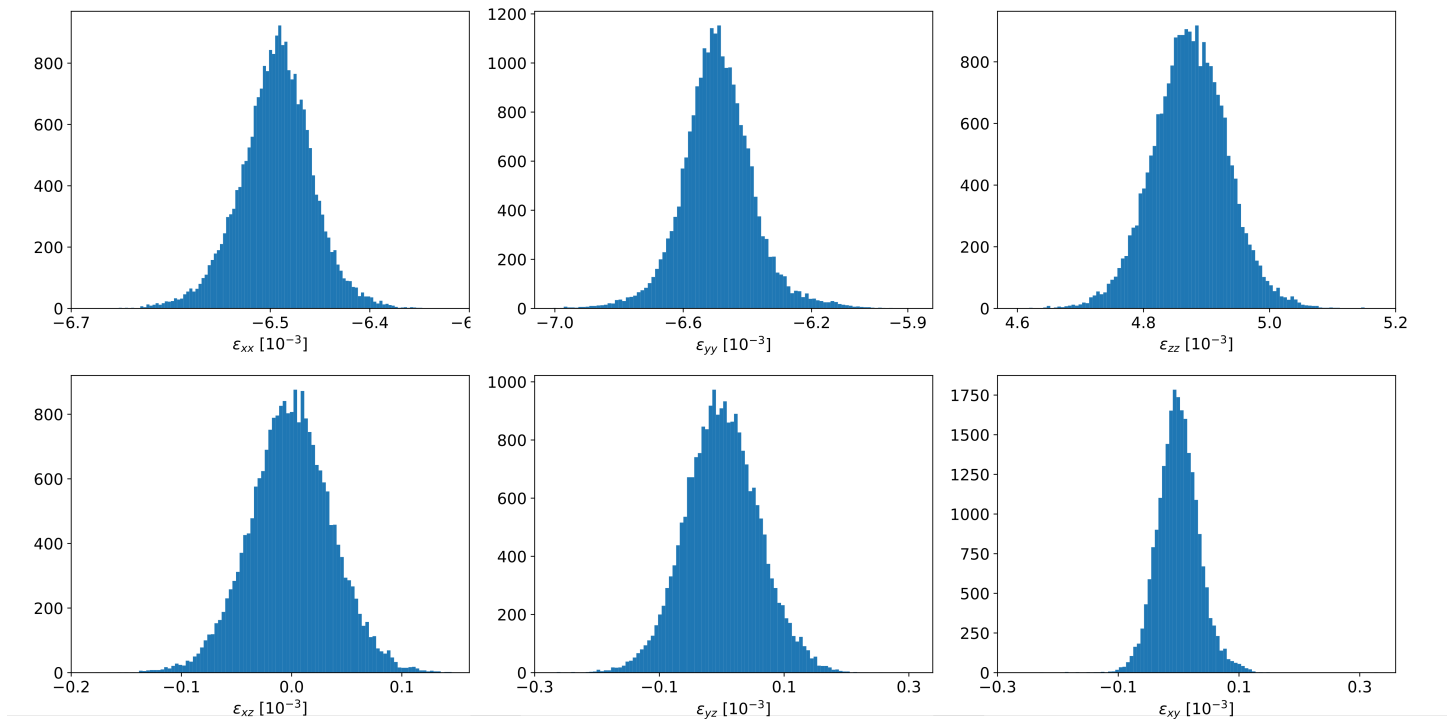
Figure S8 Histograms of the strains measured by SXDM (after filtering).

The width of the distributions is in the range of a few 10^{-4} for all components of the strain tensor, as we observed in our description of the strain maps in the main text.

The bandwidth of the long-ranged strain modulations facilitated by fluctuations of strain and composition in the SiGe buffer layer, which are described in the previous section, need to be studied for a larger field of view, since they take place over long ($> 1\,\mu m$) ranges. Thus, we demonstrate their bandwidth in Figure S9 with the histogram of the relative variation of in-plane strain measured by Raman spectroscopy mapping (Figure 6d in the main text).


Figure S9 Histogram of the in-plane strain measured by Raman spectroscopy mapping.

The width of the histogram from the Raman mapping is $> 10^{-3}$, and thus much larger compared to the SXDM histograms with only the effect of the electrodes of a few 10^{-4}. This is due to the larger bandwidth of the strain fluctuation driven by the MD network compared to the electrodes.

Atomic Force Microscopy and Cross Hatch Pattern

To investigate the surface topography of the sample, we measure Atomic Force Microscopy (AFM) in *tapping mode* on a *Bruker dimension Icon* model AFM system, obtaining a map of the surface height on an unpatterned section of the sample, shown in Figure S10.

The presence of a cross hatch pattern (CHP) on the surface is apparent, which originates from the strain and composition fluctuations in the plastically relaxed VS layers. [9;10] By observing a line cut profile across several undulations of the CHP (panel b), we note that its spatial wavelength is on the order of approx. 1 μm, matching the length scale of the long-ranged strain modulations we observed in the SXDM and Raman strain maps.
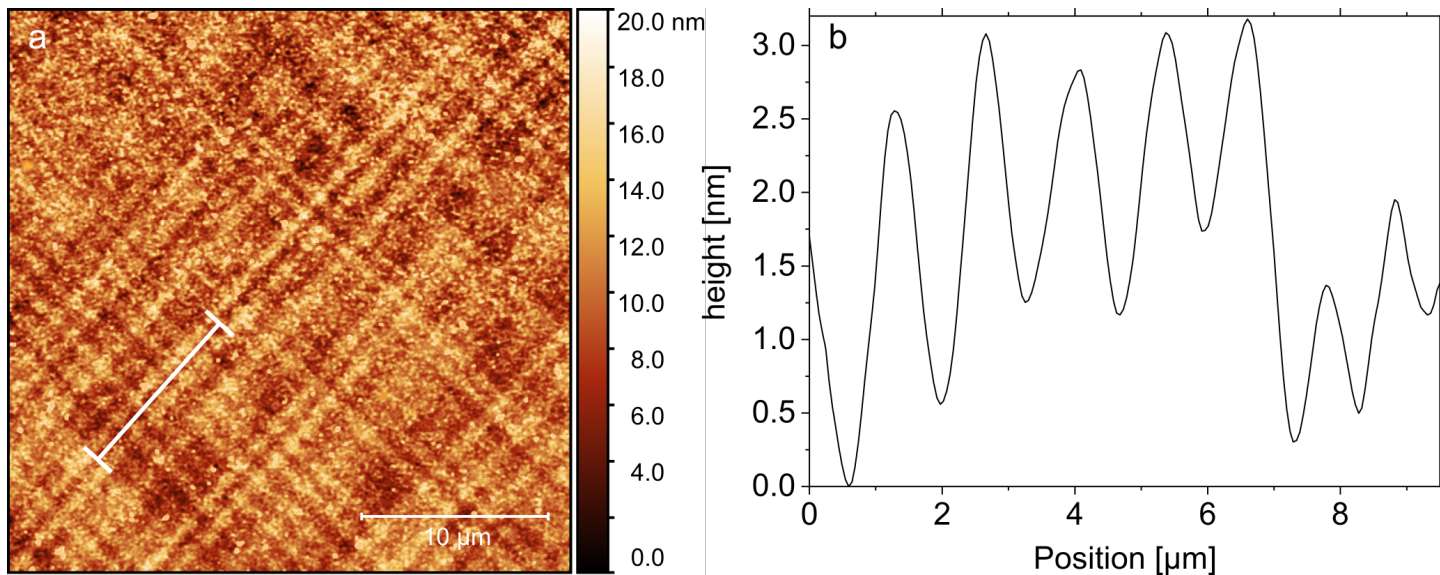

Figure S10 (a) Topography map of the cross hatch pattern on sample surface. (b) Line profile taken along the cut marked by the diagonal white bar in (a).

Thermomechanical and bandstructure simulation

In this section, we provide additional information about the simulations utilized to model the strain induced by the electrodes, and furthermore show the impact of both electrodes and dislocation networks on the HH and LH band edge energy levels.

In order to properly disentangle the CTE-induced strain from the residual thermal strain that arises from lowering the measurement temperature from room to cryogenic, all the thermomechanical simulations were performed in three dimensions on the total volume of 2 mm^3. A zero displacement boundary condition was used for the bottom surface of the simulated volume, while the metal electrodes, deposited on the top surface, are free to expand. The three electrodes present a trapezoidal cross-section whose surfaces are respectively 224, 182 and 490 μm^2, shown in Figure S11. They are all made of Palladium and their thickness is of 30 nm. Mechanical simulations rely on the elastic constants described in the previous section and on the temperature-dependent CTE. The size of the simulation was expanded and the mesh optimized to verify that boundary or finite element method conditions were not affecting the strain in the area of interest. The strain field has been obtained assuming that the three electrodes behave as a stressor with an initial pressure of 90 MPa. This last quantity has been determined comparing experimental and simulative results at room temperature. Subsequently, the thermal expansion node has been included in order to extract the mechanical deformations at cryogenic temperatures, emulating the process of cooling the device adiabatically.
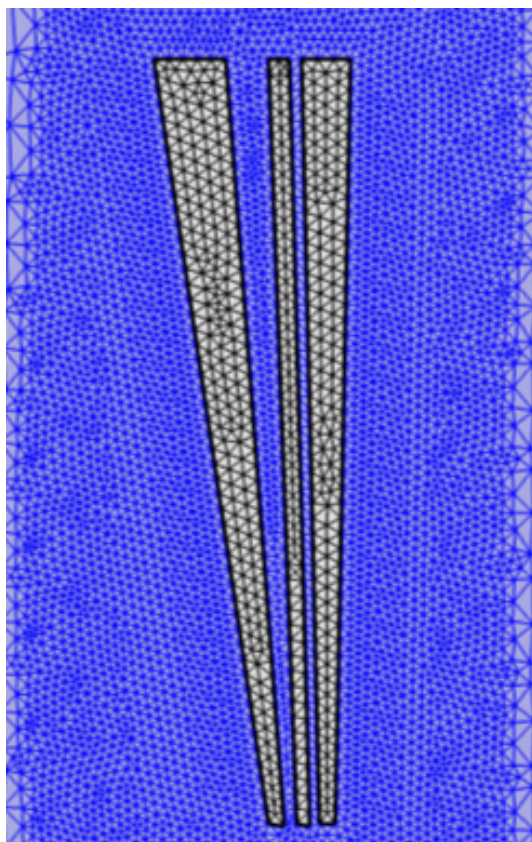

Figure S11 Metal electrode cross-section and corresponding mesh

Line cut profiles across the three electrodes for all independent components of the strain tensor obtained by the simulation at $T = 300$ K and $T = 0$ K are shown in Figure S12a-f together with the corresponding line cut from the experimental data.
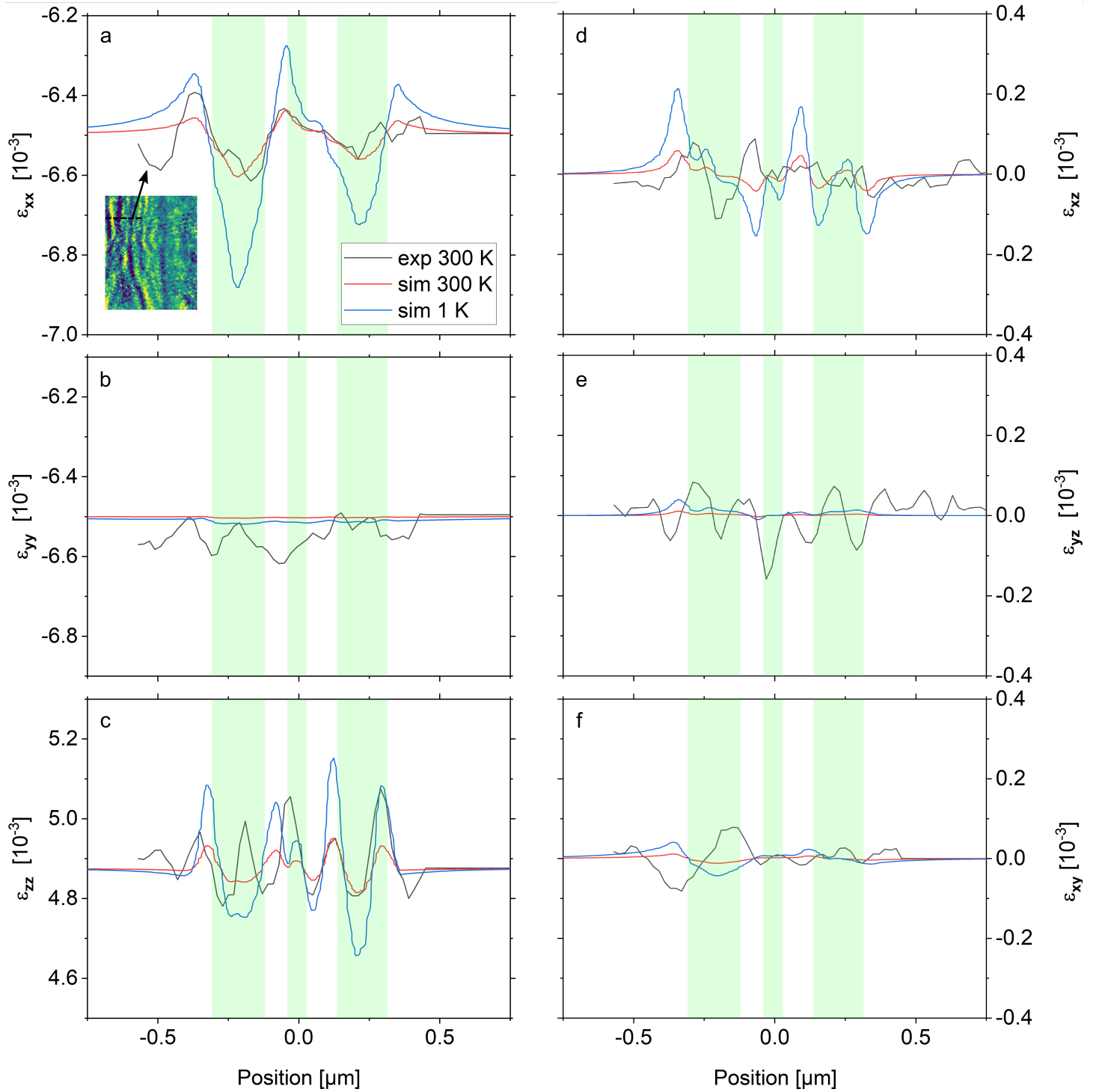
Figure S12 Profiles of all six independent strain tensor components ((a) ε_{xx}; (b) ε_{yy}; (c) ε_{zz}; (d) ε_{xz}; (e) ε_{yz}; (f) ε_{xy}) across three Pd electrodes. (black) Experimental profiles; (red) simulated at $T = 300$ K; (blue) simulated at $T = 1$ K. The inset shows where the cut was taken in the SXDM strain map. The extent of the three electrodes in the simulation is shaded in green.

To observe the influence of the electrodes on the bandstructure, local LH and HH band edge energies are calculated by bandstructure simulations, taking into account the local variations of the strain tensor (described in section 2.6 in the main text). The band edge profiles are shown in Figure S13a and b for both experimental data and simulation at 300 K and 1 K.
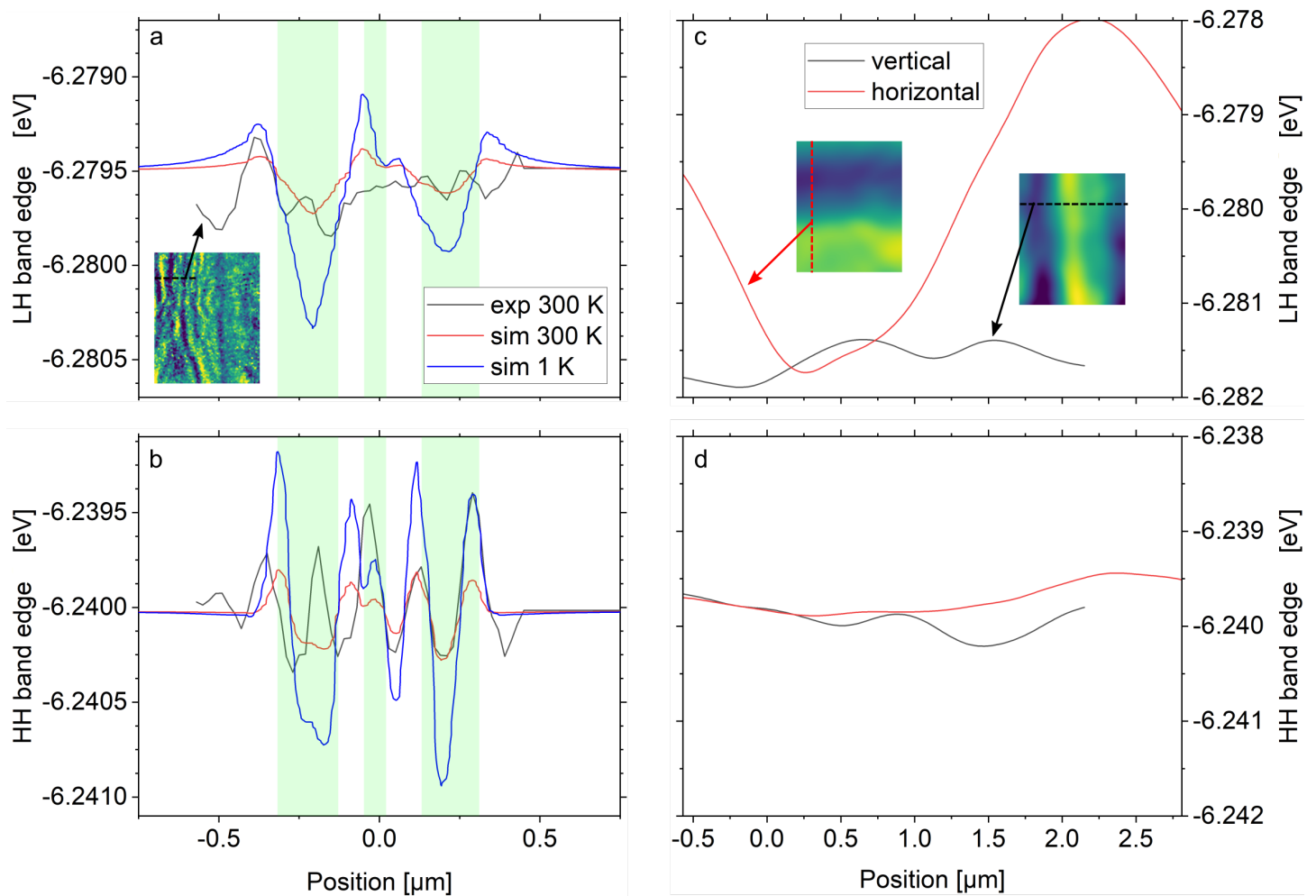
Figure S13 (a), (b) Profiles of the LH **(a)** and HH **(b)** band edge energy levels, taking into account only the effect of the electrodes and excluding the long-ranged gradients. (black) Experimental profiles; (red) simulated at $T = 300$ K; (blue) simulated at $T = 1$ K. The inset shows where the cut was taken in the SXDM strain map. The extent of the three electrodes in the simulation is shaded in green. **(c, d)** Profile of the LH **(c)** and HH **(d)** band edge energy levels along the linecuts in the two insets, including only the long-ranged strain fluctuations.

Furthermore, the effect of the long-range strain fluctuations on the band edges, excluding the more tightly localized influence of the electrodes, were calculated and are shown in Figure S13c and d. The spatial profiles of the bands were calculated along both the horizontal and the vertical axis of the map, since the long-range gradients of the strains are highly anisotropic in the mapped area. Especially the gradient of the LH band edge along the vertical axis is quite large (> 3 meV, red curve), this is caused by the strong change of ε_{yy} in this region on the sample. The Raman shift mapping (see Figure 5d in the main text) confirms, however, that gradients of a similar magnitude occur in the in-plane strain in a larger area around the device.

X-ray nanoprobe

Prior to our measurements at ID01, the X-ray nanoprobe has been characterized by means of a Ptychographic measurement of a reference object (Siemens star) in transmission mode. The reconstruction was done using the *PyNX* software package and yields amplitude and phase of the reconstructed object as well as the X-ray probe. [4] The probe field can then be propagated following wave equations, which yields the 3D distribution of X-ray intensity. The results are summarized in Figure S14. Figure S14a,b show cuts perpendicular to the two transversal directions, exposing the beam caustic and indicating a fine focus at approx. 200 μm upstream to the Siemens star. Figure S14c shows a cut perpendicular to the longitudinal direction at the focus position. Line cuts of intensity taken from this data are shown in Figure S14e, which demonstrate a beam size below 30 nm. The reconstructed region of the reference object, indicating a successful reconstruction, can be seen in Figure S14d.
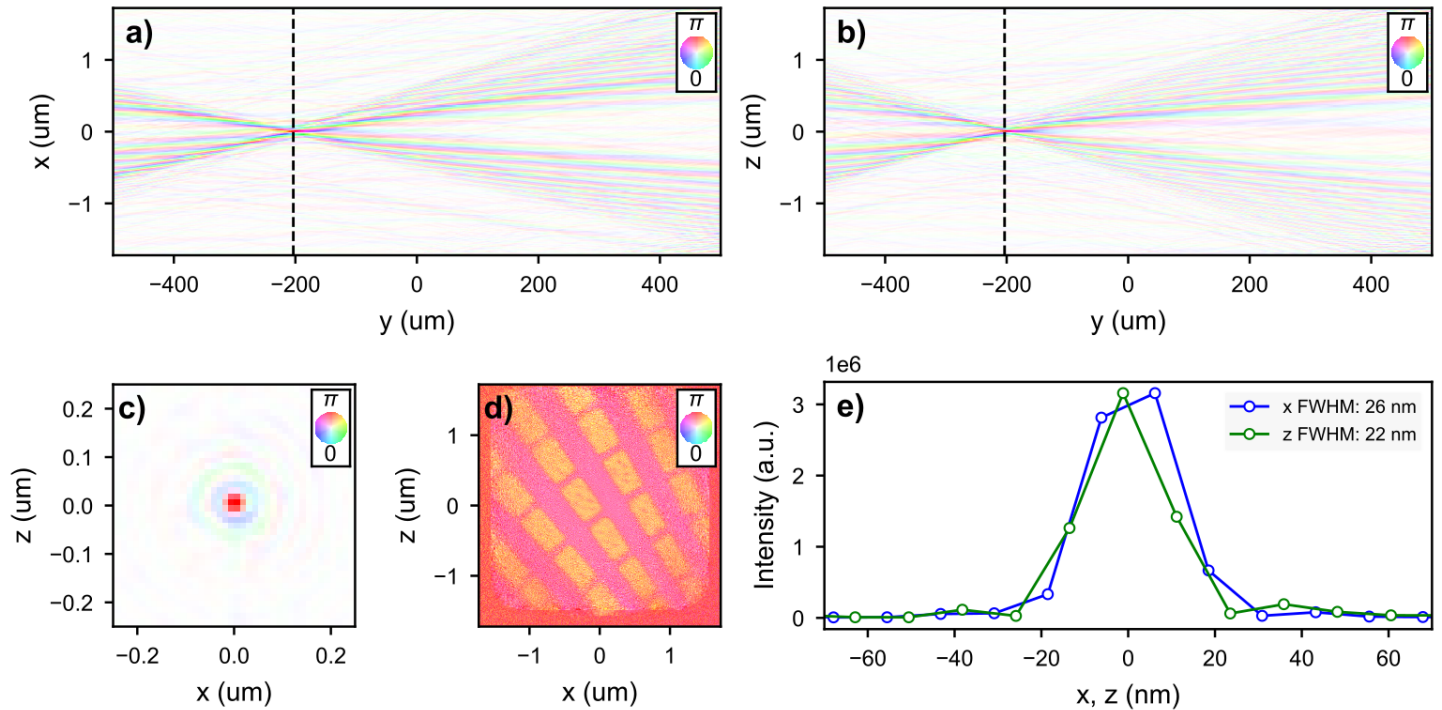
Figure S14 Ptychographic reconstruction of the beam. (a) Cut of the reconstructed beam in the xy plane; (b) cut in the yz plane; (c) cut at the beam focus position in the xz plane; (d) Reconstruction of the Siemens Star; (e) Linecuts of the beam intensity along x and z direction at the focus position.

References

[1] M. Albrecht, S. Christiansen, J. Michler, W. Dorsch, H. P. Strunk, P. O. Hansson, and E. Bauser. Surface Ripples, Crosshatch Pattern, and Dislocation Formation: Cooperating Mechanisms in Lattice Mismatch Relaxation. *Applied Physics Letters*, 67(9):1232–1234, 1995.

[2] A. P. Boresi, R. J. Schmidt, O. M. Sidebottom, et al. *Advanced Mechanics of Materials*, volume 5. Wiley New York, 1985.

[3] J. P. Dismukes, L. Ekstrom, and R. J. Paff. Lattice Parameter and Density in Germanium-silicon Alloys. *The Journal of Physical Chemistry*, 68(10):3021–3027, 1964.

[4] V. Favre-Nicolin, G. Girard, S. Leake, J. Carnis, Y. Chushkin, J. Kieffer, P. Paleo, and M.-I. Richard. PyNX: High-performance Computing Toolkit for Coherent X-ray Imaging based on Operators. *Journal of Applied Crystallography*, 53(5):1404–1413, Sept. 2020.

[5] O. Madelung. *Semiconductors — Basic Data*. Springer, 1996.

[6] C. Ponchut, J. Clément, J.-M. Rigal, E. Papillon, J. Vallerga, D. LaMarra, and B. Mikulec. Photon-counting X-ray Imaging at Kilohertz Frame Rates. *Nuclear Instruments and Methods in Physics Research Section A: Accelerators, Spectrometers, Detectors and Associated Equipment*, 576(1):109–112, June 2007.

[7] C. Richter, V. M. Kaganer, A. Even, A. Dussaigne, P. Ferret, F. Barbier, Y.-M. L. Vaillant, and T. U. Schülli. Nanoscale Mapping of the Full Strain Tensor, Rotation and Composition in Partially Relaxed $In_xGa_{1-x}N$ Layers by Scanning X-ray Diffraction Microscopy. 10.48550/ARXIV.2203.14819, 2022.

[8] A. E. Romanov, T. J. Baker, S. Nakamura, and S. J. S. Strain-induced Polarization in Wurtzite III-Nitride Semipolar Layers. *J. Appl. Phys*, 100:023522, 2006.

[9] F. Rovaris, M. H. Zoellner, P. Zaumseil, A. Marzegalli, L. Di Gaspare, M. De Seta, T. Schroeder, P. Storck, G. Schwalb, G. Capellini, and F. Montalenti. Dynamics of Crosshatch Patterns in Heteroepitaxy. *Phys. Rev. B*, 100:085307, Aug 2019.

[10] F. Rovaris, M. H. Zoellner, P. Zaumseil, M. A. Schubert, M. A., L. Di Gaspare, M. De Seta, T. Schroeder, P. Storck, G. Schwalb, C. Richter, T. U. Schülli, G. Capellini, and F. Montalenti. Misfit-dislocation Distributions in Heteroepitaxy: From Mesoscale Measurements to Individual Defects and back. *Physical Review Applied*, 10(054067), 2018.

[11] A. Sammak, D. Sabbagh, N. W. Hendrickx, M. Lodari, B. Paquelet Wuetz, A. Tosato, L. Yeoh, M. Bollani, M. Virgilio, M. A. Schubert, P. Zaumseil, G. Capellini, M. Veldhorst, and G. Scappucci. Shallow and Undoped Germanium Quantum Wells: A Playground for Spin and Hybrid Quantum Technology. *Advanced Functional Materials*, 29(14):1807613, 2019.

[12] J. J. Wortman and R. A. Evans. Young's Modulus, Shear Modulus, and Poisson's Ratio in Silicon and Germanium. *J. Appl. Phys.*, 36:153–156, 1965.

[13] M. H. Zoellner, M.-I. Richard, G. A. Chahine, P. Zaumseil, C. Reich, G. Capellini, F. Montalenti, A. Marzegalli, Y.-H. Xie, T. U. Schülli, M. Häberlen, P. Storck, and T. Schroeder. Imaging Structure and Composition Homogeneity of 300 mm SiGe Virtual Substrates for Advanced CMOS Applications by Scanning X-ray Diffraction Microscopy. *ACS applied materials & interfaces*, 7(17):9031–9037, 2015.